

Tropospheric NO₂ Measurements Using a Three-wavelength Optical Parametric Oscillator Differential Absorption Lidar

Jia Su¹, M. Patrick McCormick^{1,*}, Matthew S. Johnson², John T. Sullivan³, Michael J. Newchurch⁴, Timothy A. Berkoff⁵, Shi Kuang⁴, Guillaume P. Gronoff^{5,6}

¹Center for Atmospheric Sciences, Department of Atmospheric and Planetary Sciences, Hampton University, Hampton, Virginia 23668, USA

²Earth Science Division, NASA Ames Research Center, Moffett Field, CA, USA

³NASA Goddard Space Flight Center, Chemistry and Dynamics Laboratory, Greenbelt, MD 20771, USA

⁴Atmospheric and Earth Science Department, University of Alabama in Huntsville, Huntsville, Alabama, USA

⁵NASA Langley Research Center, Hampton, VA, 23681, USA

⁶Science Systems and Applications, Inc, VA, 23681, USA

Correspondence to: M. Patrick McCormick (PAT.MCCORMICK@HAMPTONU.EDU)

Abstract

The conventional two-wavelength Differential Absorption Lidar (DIAL) has measured air pollutants such as nitrogen dioxide (NO₂). However, high concentrations of aerosol within the planetary boundary layer (PBL) can cause significant retrieval errors using only a two-wavelength DIAL technique to measure NO₂. We proposed a new technique to obtain more accurate measurements of NO₂ using a three-wavelength DIAL technique based on an Optical Parametric Oscillator (OPO) laser. This study derives the three-wavelength DIAL retrieval equations necessary to retrieve vertical profiles of NO₂ in the troposphere. Additionally, two rules to obtain the optimum choice of the three wavelengths applied in the retrieval are designed to help increase the differences of the NO₂ absorption cross sections and reduce aerosol interference. NO₂ retrieval relative uncertainties caused by aerosol extinction, molecular

27 extinction, absorption of gases other than the gas of interest and backscattering are calculated
28 using two-wavelength DIAL (438 nm and 439.5 nm) and three-wavelength DIAL (438 nm,
29 439.5 nm and 441 nm) techniques. The retrieval uncertainties of aerosol extinction using the
30 three-wavelength DIAL technique are reduced to less than 2% of using the two-wavelength
31 DIAL technique. Moreover, the retrieval uncertainty analysis indicates that the three-wavelength
32 DIAL technique can reduce more fluctuation caused by aerosol backscattering than two-
33 wavelength DIAL technique. This study presents NO₂ concentration profiles which were
34 obtained using the HU (Hampton University) three-wavelength OPO DIAL. As a first step to
35 assess the accuracy of the HU lidar NO₂ profiles, we compared the NO₂ profiles to simulated
36 data from WRF-Chem model. This comparison suggests that the NO₂ profiles retrieved with the
37 three-wavelength DIAL technique have similar vertical structure, and magnitudes typically
38 within ± 0.1 ppb, of modeled profiles.

39 **1. Introduction**

40 Nitrogen dioxide (NO₂) plays a critical role in the tropospheric chemistry and is one of reactive
41 gases collectively referred to as “nitrogen oxides” (NO_x = nitric oxide and nitrogen dioxide (NO
42 + NO₂)) [U.S. EPA, 2018]. The sources of NO_x emissions include transportation (on-road
43 vehicles, airplanes, trains, ships), wood burning, industrial and chemical processes, activities for
44 oil and gas development, soil emissions, lightning and wildfires (see Nitrogen Oxides Emissions
45 indicator) [U.S. EPA, 2018]. Once emitted, NO reacts rapidly in the presence of ozone to form
46 NO₂. In U.S. urban locations, most measured airborne NO₂ comes from the reaction of these two
47 precursors, rather than from direct NO₂ emissions [Bertram, et al., 2005; Beirle, et al., 2011].
48 Scientific evidence indicates that short-term NO₂ exposure, ranging from 30 minutes to 24 hours,
49 can cause the exacerbation of asthma symptoms, in some cases resulting in hospitalization

50 [Berglund, et al., 1993]. Long-term NO₂ exposure is likely to have a causal relationship with
51 respiratory effects, based on evidence for the development of asthma [U.S. EPA, 2016]. And
52 NO₂ will be included in future cycles of the Global Burden of Disease as global exposure
53 estimates and evidence on their role as independent risk factors accumulates [Larkin et al., 2017].
54 Additionally, atmospheric processing of NO₂ leads to the formation of nitrogen-bearing particles
55 that can eventually deposit to the surface, causing acidification, nitrogen enrichment, and other
56 ecological effects [Russell et al., 2012]. Local or global NO₂ monitoring is essential for
57 understanding atmospheric chemistry as well as for human-health and environmental
58 management and control.

59 Measurements of the intensity of ultraviolet or visible absorption spectra from the ground or
60 from satellites are commonly used to retrieve the column density of NO₂ [Celarier et al., 2008;
61 Valks et al., 2011; Berg et al., 2012]. Satellite-based instruments such as Ozone Monitoring
62 Instrument (OMI), Global Ozone Monitoring Experiment (GOME and GOME-2) and SCanning
63 Imaging Absorption SpectroMeter for Atmospheric CHartographY (SCIAMACHY) can provide
64 global scale NO₂ column measurements during daytime [Boersma et al., 2008; Bucsela et al.,
65 2008]. Moreover, plumes of NO₂ by cities, power plants, and even ships can be tracked using the
66 recent high spatial resolution observations of NO₂ from TROPOMI on Sentinel-5P since 2017
67 [Lorente, et al., 2019; Georgoulias et al., 2020]. However, they are unable to obtain local high
68 temporal resolution NO₂ emissions such as variations in hourly NO₂ concentrations due to their
69 long repeat cycle, since the lifetime of tropospheric NO₂ is only about 6 hour in summer and 18-
70 24 hours in winter due to photochemical effect [Beirle, et al., 2003; Cui et al., 2016]. In addition,
71 measurements of tropospheric NO₂ from satellite or aircraft are also influenced and limited by
72 clouds [Bovensmann et al., 1999; Liang et al., 2017]. Ground-based measurements of column

73 NO₂ from instruments such as Pandora using differential optical absorption spectroscopy (DOAS)
74 are often used for the validation of satellite instruments [Herman et al., 2009; Lamsal et al., 2014;
75 Kollonige et al., 2018]. In situ measurements of near-surface NO₂ can best monitor local
76 emissions. However, at this point in time, they cannot provide vertically-resolved measurements.
77 Balloon measurements using a NO₂-sonde can produce vertical profiles, but these measurements
78 are very limited in time and space, especially in the Southern Hemisphere. The primary source of
79 data on the vertical distribution of NO₂ comes from operational sites around the world. However,
80 their operation can be expensive and labor-intensive. [Scott et al., 1999; Herman et al., 2009;
81 Sluis et al., 2010].

82 The DIAL technique offers the potential for autonomous, 24x7 operation, with improved
83 temporal resolution. Absorption of light by molecules is the basis for DIAL and numerous
84 atmospheric constituents absorbing light. Conventional DIAL operates at two absorbing
85 wavelengths, one stronger than the other indicated by on (λ_{on}) and off (λ_{off}) wavelength of the
86 gaseous absorption feature of interest. Because of different absorption at λ_{on} and λ_{off} , the
87 difference between the backscattered laser signals at the two wavelengths can be used to derive
88 the number density of the absorption gas. Taking the log-ratio of these returns at closely spaced
89 wavelengths removes system parameters and attenuation to and from the target of interest [Rothe
90 et al., 1974; Sullivan et al., 2014]. Thus, this technology provides measurements of the
91 concentration of gas, such as NO₂, O₃, and SO₂ at a particular location and time [Fredriksson et
92 al., 1984; Newchurch et al., 2003; Kuang et al., 2013; Sullivan et al., 2017]. The DIAL technique
93 provides the unique capability of remotely monitoring urban/rural area localized NO₂
94 concentrations/emissions and profiling their tropospheric vertical NO₂ concentration. However,
95 aerosols are abundant within the PBL and can cause significant retrieval errors in a two-

96 wavelength DIAL technique to measure NO₂. To better understand this aerosol problem and
 97 produce a more accurate NO₂ profile measurement, we described a new technique using a three-
 98 wavelength DIAL technique based on the intrinsic capabilities of using a multi-wavelength OPO
 99 laser system. HU has incorporated an OPO laser into its lidar system. The OPO laser enables
 100 researchers to optimize (tune) wavelength choices for specific measurements [P.Weibring et al.,
 101 2003]. The three-wavelength DIAL retrieval equations are derived in this study. Our optimum
 102 choices for the three wavelengths to be used for our NO₂ retrievals are designed to help increase
 103 the difference in NO₂ absorption cross section, and reduce aerosol influence. NO₂ retrieval
 104 relative uncertainties are calculated using the two-wavelength DIAL (438 nm and 439.5 nm) and
 105 the three-wavelength DIAL (438 nm, 439.5 nm and 441 nm). Tropospheric NO₂ profiles were
 106 obtained by applying the proposed technique to HU OPO DIAL lidar. As a first-order assessment,
 107 the HU lidar results were compared with simulated data from the WRF-Chem air quality model.

108 **2. Method**

109 To minimize aerosols-interference on the retrievals of NO₂, a three-wavelength DIAL technique
 110 was proposed with $\lambda_1 < \lambda_2 < \lambda_3$. Table 1 shows expressions for the extinction and backscatter of
 111 molecules and aerosols for these three wavelengths. In Table 1, β_m and β_a are backscatter from
 112 molecules and aerosols for the wavelength of λ_2 ; α_m and α_a are the extinction of molecules and
 113 aerosols for the wavelength of λ_2 ; e is the aerosol Ångström exponent and assumed to be equal
 114 for the three wavelengths because the three wavelengths are very close.

Table 1. Extinction and backscatter of molecule and aerosol for wavelengths of λ_1 , λ_2 and λ_3 .

wavelength	Molecular backscattering	Aerosol backscattering	Molecular extinction	Aerosol extinction
λ_1	$\left(\frac{\lambda_1}{\lambda_2}\right)^{-4} \beta_m$	$\left(\frac{\lambda_1}{\lambda_2}\right)^{-e} \beta_a$	$\left(\frac{\lambda_1}{\lambda_2}\right)^{-4} \alpha_m$	$\left(\frac{\lambda_1}{\lambda_2}\right)^{-e} \alpha_a$
λ_2	β_m	β_a	α_m	α_a

λ_3	$\left(\frac{\lambda_3}{\lambda_2}\right)^{-4} \beta_m$	$\left(\frac{\lambda_3}{\lambda_2}\right)^{-e} \beta_a$	$\left(\frac{\lambda_3}{\lambda_2}\right)^{-4} \alpha_m$	$\left(\frac{\lambda_3}{\lambda_2}\right)^{-e} \alpha_a$
-------------	---	---	--	--

The three elastic lidar equations can be expressed as:

$$X(\lambda_1, Z) = C_1 \frac{\left[\left(\frac{\lambda_1}{\lambda_2}\right)^{-4} \beta_m(Z) + \left(\frac{\lambda_1}{\lambda_1}\right)^{-e} \beta_a(Z)\right]}{Z^2} \exp\left\{-2 \int_0^Z \left[\left(\frac{\lambda_1}{\lambda_2}\right)^{-4} \alpha_m(z) + \left(\frac{\lambda_1}{\lambda_1}\right)^{-e} \alpha_a(z) + \sigma_N(\lambda_1, z) N_N(z) + O_{abs}(\lambda_1, z)\right] dz\right\} \quad (1)$$

$$X(\lambda_2, Z) = C_2 \frac{[\beta_m(Z) + \beta_a(Z)]}{Z^2} \exp\{-2 \int_0^Z [\alpha_m(z) + \alpha_a(z) + \sigma_N(\lambda_2, z) N_N(z) + O_{abs}(\lambda_2, z)] dz\} \quad (2)$$

$$X(\lambda_3, Z) = C_3 \frac{\left[\left(\frac{\lambda_3}{\lambda_2}\right)^{-4} \beta_m(Z) + \left(\frac{\lambda_3}{\lambda_2}\right)^{-e} \beta_a(Z)\right]}{Z^2} \exp\{-2 \int_0^Z \left[\left(\frac{\lambda_3}{\lambda_2}\right)^{-4} \alpha_m(z) + \left(\frac{\lambda_3}{\lambda_2}\right)^{-e} \alpha_a(z) + \sigma_N(\lambda_3, z) N_N(z) + O_{abs}(\lambda_3, z)\right] dz\} \quad (3)$$

115 where X is the lidar signal; C_1 , C_2 and C_3 are lidar constants; the subscripts a and m represent
 116 aerosol, and molecule, respectively; σ_N is the absorption cross section for the gas of interest; N_N
 117 is the molecular density of the gas of interest; O_{abs} is absorption of gases other than the gas of
 118 interest and z is the altitude. The molecular density of the gas of interest can be obtained using
 119 Eq. (1), (2) and (3).

120 NO_2 density retrieval equation can be expressed as:

$$121 \quad N_N(Z) = \frac{\frac{1}{2} \times \frac{d}{dz} \left[\ln \frac{X(\lambda_1, Z) X(\lambda_3, Z)}{X(\lambda_2, Z)^2} \right] - AED(Z) - MED(Z) - OAD(Z) - B(Z)}{\Delta \sigma_N} \quad (4)$$

$$122 \quad \Delta \sigma_N = 2\sigma_N(\lambda_2) - \sigma_N(\lambda_1) - \sigma_N(\lambda_3) \quad (5)$$

$$123 \quad B(Z) = \frac{1}{2} \frac{d}{dz} \left[\ln \frac{\left[\left(\frac{\lambda_3}{\lambda_2}\right)^{-4} \beta_m(Z) + \left(\frac{\lambda_3}{\lambda_2}\right)^{-e} \beta_a(Z)\right] \left[\left(\frac{\lambda_1}{\lambda_2}\right)^{-4} \beta_m(Z) + \left(\frac{\lambda_1}{\lambda_2}\right)^{-e} \beta_a(Z)\right]}{[\beta_m(Z) + \beta_a(Z)]^2} \right] \quad (6)$$

$$124 \quad AED(z) = K \alpha_a(Z) \quad K = 2 - \left(\frac{\lambda_1}{\lambda_2}\right)^{-e} - \left(\frac{\lambda_3}{\lambda_2}\right)^{-e} \quad (7)$$

$$125 \quad MED(z) = \left[2 - \left(\frac{\lambda_1}{\lambda_2}\right)^{-4} - \left(\frac{\lambda_3}{\lambda_2}\right)^{-4} \right] \alpha_m(Z) \quad (8)$$

$$126 \quad OAD(z) = 2O_{abs}(\lambda_2, z) - O_{abs}(\lambda_1, z) - O_{abs}(\lambda_3, z) \quad (9)$$

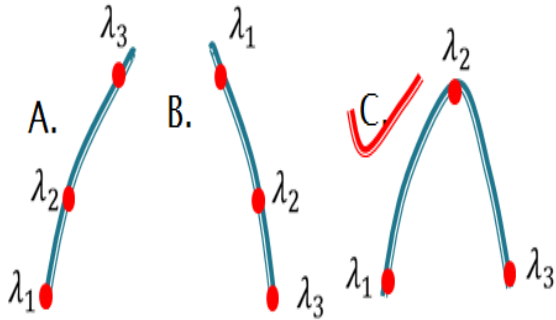
127 where AED, MED, OAD and B are the correction terms of aerosol extinction, molecular
 128 extinction, absorption of gases other than the gas of interest and backscattering, respectively.
 129 Because the atmospheric molecular density is relatively stable, MED can be corrected using a
 130 numerical model or local real-time radiosonde data. OAD can be removed by choosing

131 appropriate wavelengths. However, aerosol is variable especially in PBL. For correction of AED
132 and B, we need accurate aerosol measurements. However, accurate aerosol measurements are not
133 easily to be obtained. From the above NO₂ retrieval relative equation, all of correction terms are
134 related to the three wavelengths, so how to choose the three wavelengths is very critical to
135 reduce correction terms and improve the accuracy of NO₂ retrievals. We designed two rules to
136 obtain the optimum choice for the three wavelengths:

137 **a.** The chosen three wavelengths increase differences of the NO₂ absorption cross section ($\Delta\sigma_N$)
138 to improve NO₂ retrieval.

139 According to Eq. (4), the more $\Delta\sigma_N$ is, the less all of correction terms are. So the chosen three
140 wavelengths should help to increase $\Delta\sigma_N$. Generally, researchers only used an increasing
141 absorption method ($\sigma_N(\lambda_1) < \sigma_N(\lambda_2) < \sigma_N(\lambda_3)$) or a decreasing absorption method ($\sigma_N(\lambda_1) >$
142 $\sigma_N(\lambda_2) > \sigma_N(\lambda_3)$) (illustrated in Fig. 1) to choose the three wavelengths [Wang, et al., 1997; Liu, et
143 al., 2017]. Wang used three wavelengths corresponding to the strong, medium and weak
144 absorption of O₃ to obtain an accurate stratospheric ozone profile in the presence of volcanic
145 aerosols. Liu used three wavelengths of 448.10nm, 447.20nm and 446.60 nm corresponding to
146 the strong, medium and weak absorption of NO₂ to retrieve NO₂. Equation (10) and (11) are
147 calculated values of $\Delta\sigma_N$ for the increasing absorption method and the decreasing absorption
148 method using Eq. (5). Using the increasing absorption method and the decreasing absorption
149 method to choose the three wavelengths, the values of $\Delta\sigma_N$ are both decreased according to Eq.
150 (10) and (11) compared to the conventional two-wavelength DIAL technique. According to
151 characteristics of the NO₂ absorption spectrum showed in Fig. 2, a bumping absorption method
152 ($\sigma_N(\lambda_1) < \sigma_N(\lambda_2) \& \sigma_N(\lambda_3) < \sigma_N(\lambda_2)$) is designed to choose the three wavelengths which can
153 increase value of $\Delta\sigma_N$ compared to the two-wavelength DIAL technique according to Eq. (12).

154 However, for DIAL systems to measure other atmospheric gases like ozone, it is only practical to
 155 use wavelength selection Method B because of the shape of the ozone absorption spectrum
 156 (lacking narrow peaks).



157 Fig.1 The three-wavelength chosen methods:
 158 Increasing absorption method (A), Decreasing
 159 absorption method (B) and Bumping absorption
 160 method (C)
 161
 162

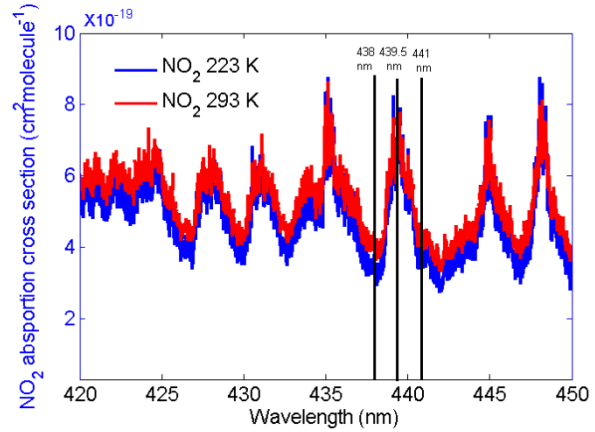


Fig.2 NO₂ strong absorption cross section
 between 420 nm and 450 nm

163 Increasing absorption method: $\Delta\sigma_N = abs[\sigma_N(\lambda_2) - \sigma_N(\lambda_1)] - abs[\sigma_N(\lambda_2) - \sigma_N(\lambda_3)]$
 164 (10)

165 Decreasing absorption method: $\Delta\sigma_N = abs[\sigma_N(\lambda_2) - \sigma_N(\lambda_3)] - abs[\sigma_N(\lambda_2) - \sigma_N(\lambda_1)]$
 166 (11)

167 Bumping absorption method: $\Delta\sigma_N = abs[\sigma_N(\lambda_2) - \sigma_N(\lambda_1)] + abs[\sigma_N(\lambda_2) - \sigma_N(\lambda_3)]$
 168 (12)

169 **b.** The chosen three wavelengths can reduce or remove AED.

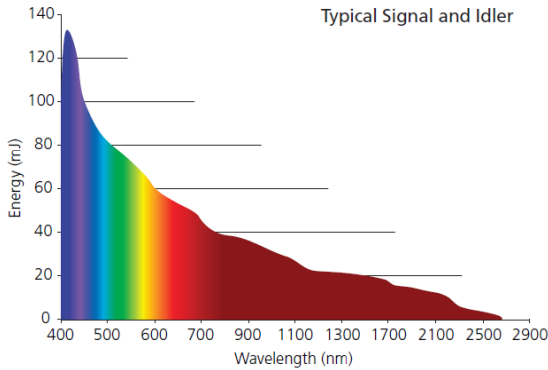
170 It means the value of AED is equal or close to 0. Choosing the appropriate three wavelengths to
 171 make the value of K in Eq. (12) equal or close to 0, the value of AED will be equal or close to 0.

172 The value of K in Eq. (12) changes with different aerosol Ångström exponents. For example, to
 173 remove boundary layer aerosol influence, we can set aerosol Ångström exponents=1 to calculate

174 the value of K to choose the three wavelengths because the size of aerosol in the boundary layer
 175 is typically large [Schuster, et al., 2006].

176 **3. HU three-wavelength OPO DIAL system**

Horizon performance with PL 8000 Pump



Description	
Pulsewidth (nsec)	3-7
Pointing Stability (urad)	<±100
Linewidth (cm ⁻¹)	
Unseeded	3-7
Doubling/Mixing	<10
Energy Stability (% 99% of shots)	<±10
Divergence (mrad, FWHM)	<2 (both axes)
Beam Diameter (mm, near field)	4-7
Beam Roundness (% near field)	>85
Polarization (%)	
Signal Horizontal	>99
Idle Horizontal	>99

177

178 Fig.3 Continuum Horizon II energy outputs (a) and parameters (b) with PL 8000 pump

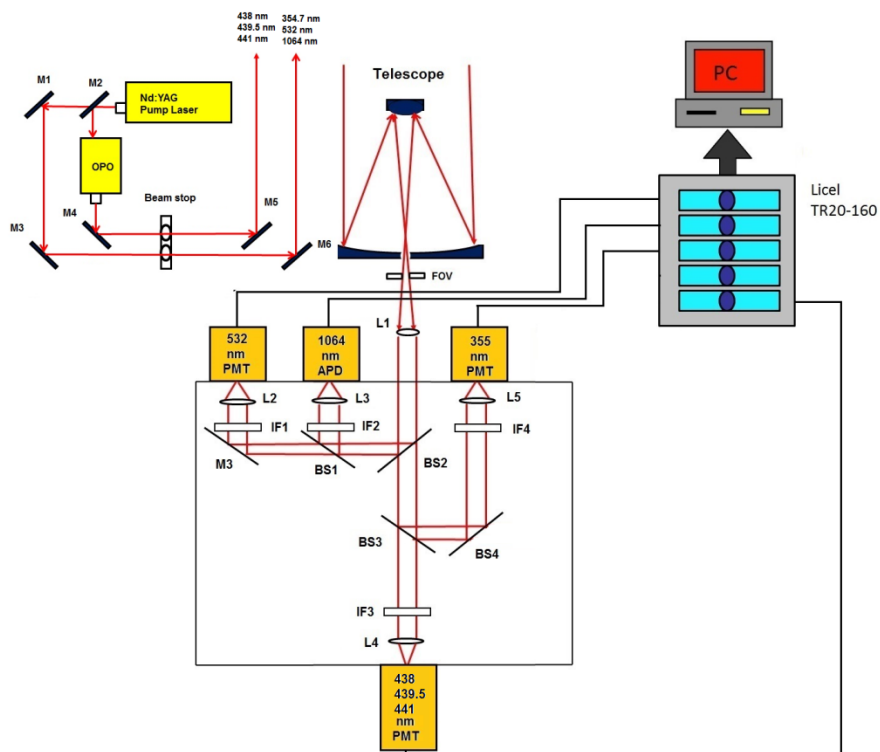
179 The HU lidar is located on the campus of HU (37.02° N, 76.34° W) in Hampton, VA. A
 180 Continuum Horizon II tunable OPO laser and a Continuum Powerlite DLS 8000 pump laser have
 181 recently been incorporated into HU lidar system. The OPO laser enables researchers to optimize
 182 (tune) the wavelength choices and provides more flexibility than fixed-frequency wavelength
 183 shifters such as Raman cells. The wavelength tuning range of our OPO extends from 192 nm to
 184 2750 nm. This range is fully automated with precision scanning for true hands-free operation.
 185 Fig. 3(a) and (b) show the Continuum Horizon II output energy and its parameters. The OPO
 186 laser energy outputs between 400 nm and 500 nm which overlap with the NO₂ strong absorption
 187 spectral zone in Fig. 2 produce near the maximum possible power in the spectrum. Combining
 188 the OPO laser energy outputs, NO₂ absorption spectral and two three-wavelength chosen rules,
 189 438 nm, 439.5 nm and 441 nm shown in Fig. 2 result in the wavelengths of HU three-wavelength
 190 DIAL system because $\Delta\sigma_N$ of the three-wavelength pair is more than other three-wavelength

191 pairs in NO₂ strong absorption spectral zone and the K value of the three-wavelength is 0.000023
192 (close to 0). The HU lidar system currently consists of a Continuum OPO laser system as the
193 light source, a 48-inch non-coaxial Cassegrainian-configured telescope receiver, a light
194 separation system that uses beam splitters and interference filters, a detecting system including
195 photomultiplier tubes (PMT) and avalanche photodiodes (APDs) and a Licel optical transient
196 recorder. A schematic of the lidar system is shown in Fig.4. The system can be configured to
197 measure multi-wavelength aerosols and NO₂ density. High-resolution backscatter measurements
198 extend from the boundary layer (1.2 km) to free troposphere. The pump laser operates at three
199 fixed wavelengths (1064, 532, and 354.7 nm). The 354.7-nm laser is mostly reflected into OPO
200 laser to produce three-wavelength (338 nm, 339.5 nm and 441 nm). Steering mirrors whose axes
201 are aligned with a receiving telescope axis directs these laser outputs into the atmosphere. The
202 laser backscatter is collected by a 48-inch diameter telescope and split into specific wavelength
203 bands by a beam separation unit, which combines filters and beam-splitters for dispersion of the
204 return backscatter to various detection channels. Using filters and beam-splitters makes the
205 beam-splitting system simple, compact, and easy to change or add other spectral channels for
206 other measurements. Currently, wavelengths of 438 nm, 439.5 nm, 441 nm, 354.7 nm, 532 nm
207 and 1064 nm are focused to PMTs and APD, and recorded by a Licel data-collecting system for
208 measurements of aerosol, and NO₂.

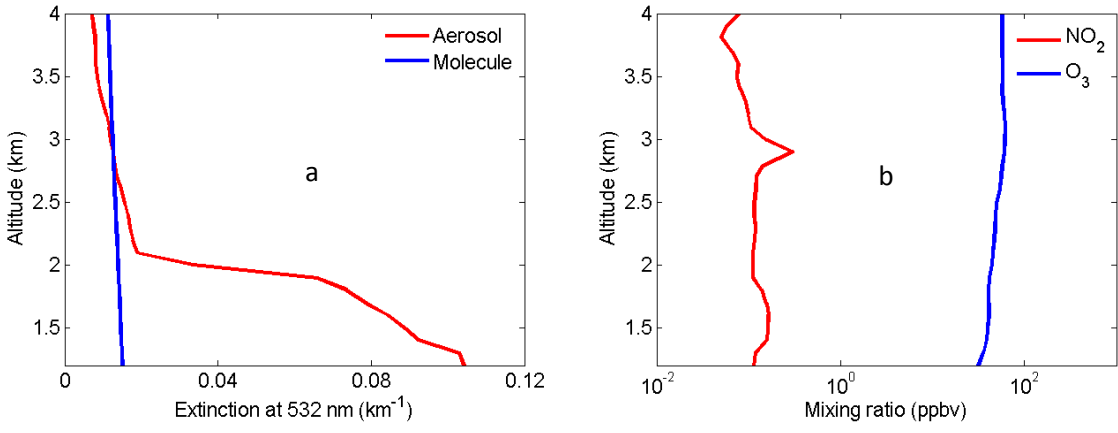
209 To demonstrate that the HU three-wavelength OPO DIAL system can effectively reduce aerosol
210 influence and accurately retrieve NO₂, retrieval correction terms of AED, MED, OAD and B in
211 Eq. (4) are simulated using two-wavelength DIAL technique (438 nm and 439.5 nm) and the
212 three-wavelength DIAL technique (438 nm, 439.5 nm and 441 nm). Ozone was used for the
213 simulation of OAD because only ozone absorption can produce a little influence on NO₂ retrieval

214 based on HITRAN 1.1.2.0 database. Atmospheric data of aerosol, molecule, O₃ and NO₂ for
215 these simulations are from the HU local lidar aerosol measurements, radiosonde, NASA
216 Tropospheric Ozone Lidar Network (TOLNet) and NASA Deriving Information on Surface
217 Conditions from COLUMN and VERTically Resolved Observations Relevant to Air Quality
218 (DISCOVER-AQ) measurements shown in Fig.5. Extinction and backscatter of aerosol at 438
219 nm, 439.5 nm and 441 nm can be calculated from aerosol extinction profile at 532 nm in Fig.5 (a)
220 with the setting of lidar ratio=50 and $e=1, 2$ and 3. Lidar ratio is wavelength dependent and its
221 value in the visible band is in general smaller than in the UV band for the same type of aerosols
222 [Kuang et al., 2020; Reid et al., 2017]. Absorption of NO₂ and O₃ at 438 nm, 439.5 nm and 441
223 nm can be calculated using their mixing ratio profiles in Fig.5 (b) and their absorption cross-
224 sections from HITRAN 1.1.2.0 database. MED, AED, OAD, B and absorption difference of NO₂
225 (NAD) are simulated using two-wavelength DIAL technique with different aerosol Ångström
226 exponents ($e=1, 2$ and 3) shown in Fig. 6 (a), (c) and (e), and the three-wavelength DIAL
227 technique shown in Fig.6 (b), (d) and (f). In Fig. 6, red lines are NAD; black lines are MED;
228 deep blue lines are AED; light blue lines are OAD. In Fig. 6, all OAD is far less than NAD. It is
229 concluded that ozone absorption has negligible influence on the retrieval of NO₂. In Fig. 6 (a), (c)
230 and (d), MED and AED in PBL are both more than NAD using the two-wavelength DIAL
231 technique. Because atmospheric molecules are relatively stable, MED can be corrected using
232 local model or real-time radiosonde data. However, aerosol is variable, so aerosols are a
233 significant uncertainty for retrieving NO₂ with the conventional two-wavelength DIAL technique.
234 In Fig. 6 (b), (d) and (f), MED and AED in boundary layer are both much smaller than NAD
235 using proposed three-wavelength DIAL technique. It is proven that three-wavelength DIAL
236 technique can effectively decrease retrieval errors caused by aerosol extinction. From Fig.5, we

237 can see AED using three-wavelength DIAL technique can be reduced to less than 2% of AED
 238 using two-wavelength DIAL technique at least. Therefore, even if AED is not corrected, NO₂
 239 still can be accurately retrieved. Moreover, simulated B using the two-wavelength DIAL
 240 technique and the three-wavelength DIAL technique are shown in Fig. 6 with green lines. The
 241 sharp change on vertical adjacent aerosol backscatter can cause drastic changes of B term. In Fig.
 242 6, the value of B term using three-wavelength DIAL technique is far less than using two-
 243 wavelength DIAL technique. So the three-wavelength DIAL technique can reduce more
 244 fluctuation caused by aerosol backscattering than two-wavelength DIAL technique.

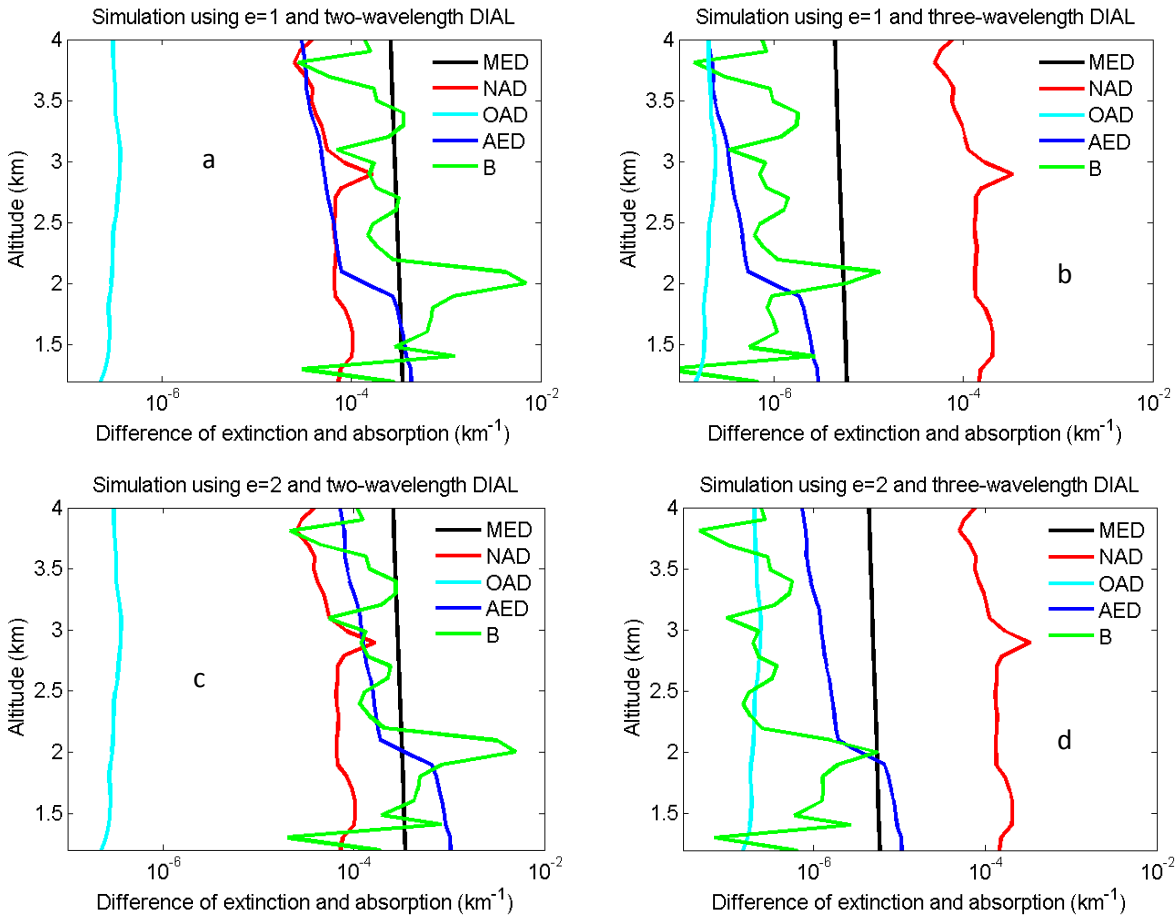


245
 246 Fig.4 HU lidar system (L-lens, M-mirror, BS-beam-splitter, IF-interference filter, FOV-field of view,
 247 PMT-Photomultiplier tube, APD-Avalanche Photodetector)



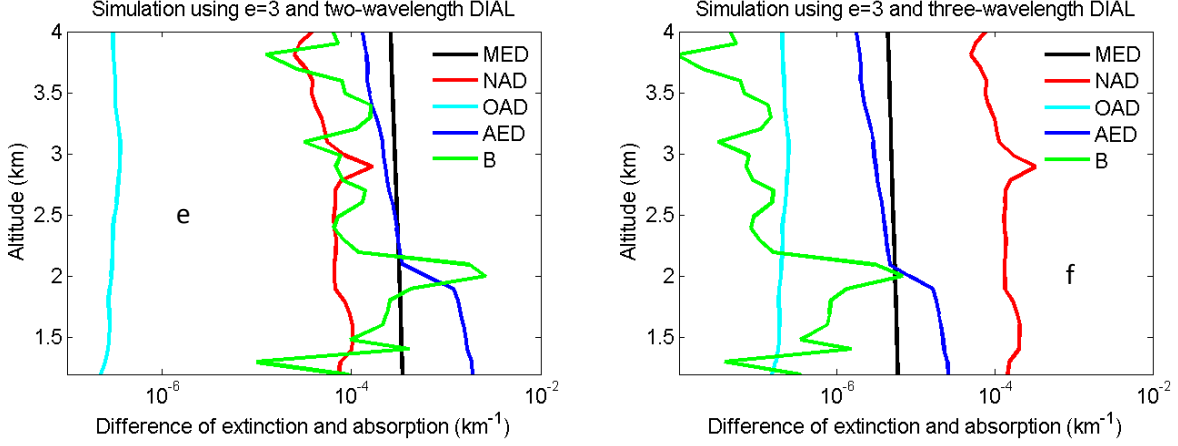
248

249 Fig.5 Atmospheric profiles used for modeling NO₂ lidar correction terms. (a) Aerosol extinction profile
 250 (red) at 532 nm measured by the HU lidar and molecular extinction profile (blue) at 532 nm derived from
 251 local radiosonde data; (b) NO₂ (red) and O₃ (blue) mixing ratio profiles from NASA DISCOVER-AQ
 252 and TOLNet.



253

254



255

256 Fig.6 Simulated MED (black), NAD (red), OAD (light blue), AED (deep blue)and B (green) using two-
 257 wavelength DIAL with e=1(a), e=2 (c) and e=3 (e) and three-wavelength DIAL technique with e=1(b),
 258 e=2(d) and e=3(f).

259

260 4. Uncertainty analysis

261 According to NO₂ retrieval Eq.4, the NO₂ measurement uncertainty is due to molecule,
 262 absorption of gases other than the gas of interest, aerosol and noise of lidar signals. The total
 263 relative uncertainty can be expressed as Eq. (13) [Leblanc et al., 2016].

$$264 \quad U_{NO_2}(z) = \sqrt{U_{AED}(z)^2 + U_{MED}(z)^2 + U_{OAD}(z)^2 + U_B(z)^2 + U_S(z)^2} \quad (13)$$

$$265 \quad U_{MED}(z) = \frac{u[MED(z)]}{N_N(z)\Delta\sigma_N} = \frac{\left[2 - \left(\frac{\lambda_2}{\lambda_1}\right)^4 - \left(\frac{\lambda_2}{\lambda_3}\right)^4\right]u[\alpha_m(z)]}{N_N(z)\Delta\sigma_N} = \frac{\left[2 - \left(\frac{\lambda_2}{\lambda_1}\right)^4 - \left(\frac{\lambda_2}{\lambda_3}\right)^4\right]\sigma_m u[N_m(z)]}{N_N(z)\Delta\sigma_N} \quad (14)$$

266

$$267 \quad U_{OAD}(z) = \frac{u[OAD(z)]}{N_N(z)\Delta\sigma_N} = \frac{u[2O_{abs}(\lambda_2,z) - O_{abs}(\lambda_1,z) - O_{abs}(\lambda_3,z)]}{N_N(z)\Delta\sigma_N} = \frac{[2\sigma_o(\lambda_2,z) - \sigma_o(\lambda_1,z) - \sigma_o(\lambda_3,z)]u[N_o(z)]}{N_N(z)\Delta\sigma_N} \quad (15)$$

268

$$269 \quad U_{AED}(z) = \frac{u[AED(z)]}{N_N(z)\Delta\sigma_N} = \frac{\left[2 - \left(\frac{\lambda_2}{\lambda_1}\right)^e - \left(\frac{\lambda_2}{\lambda_3}\right)^e\right]u[\alpha_a(z,s)]}{N_N(z)\Delta\sigma_N} \quad (16)$$

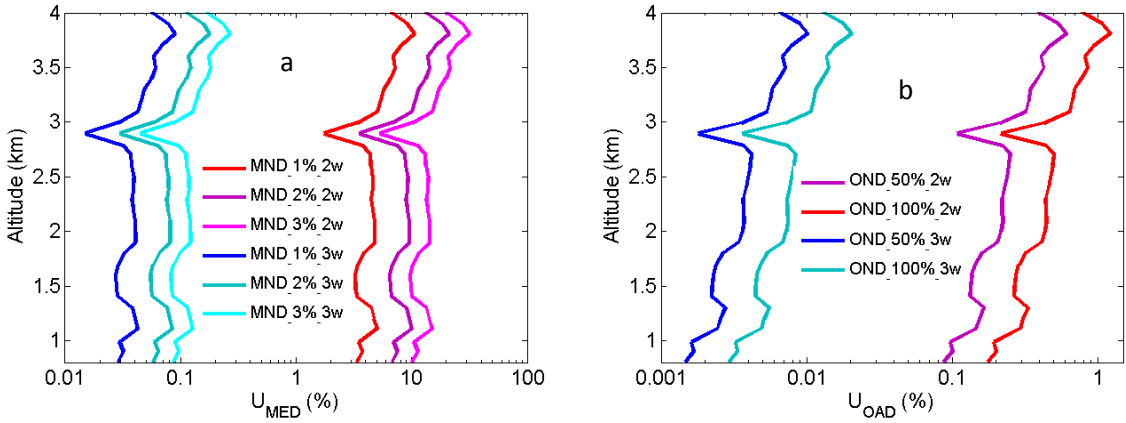
$$270 \quad U_B(z) = \frac{u\left\{\frac{1}{2} \frac{d}{dz} \ln \left[\frac{\left[\left(\frac{\lambda_2}{\lambda_3}\right)^4 \beta_m(z) + \left(\frac{\lambda_2}{\lambda_3}\right)^e \beta_a(z,s)\right] \left[\left(\frac{\lambda_2}{\lambda_1}\right)^4 \beta_m(z) + \left(\frac{\lambda_2}{\lambda_1}\right)^e \beta_a(z,s)\right]}{[\beta_m(z) + \beta_a(z,s)]^2} \right]\right\}}{N_N(z)\Delta\sigma_N} \quad (17)$$

$$\begin{aligned}
271 \quad U_S(z) &= \frac{u\left\{\frac{1}{2} \times \frac{d}{dz} \left[\ln \frac{X(\lambda_1, Z)(\lambda_3, Z)}{X(\lambda_2, Z)^2} \right] \right\}}{N_N(Z) \Delta \sigma_N} = \\
272 \quad &\frac{\frac{1}{2} \times \left\{ \frac{d\left\{ \frac{d}{dz} \left[\ln \frac{X(\lambda_1, Z)(\lambda_3, Z)}{X(\lambda_2, Z)^2} \right] \right\}}{d[X(\lambda_1, Z)]} \times u[X(\lambda_1, Z)] \right\}^2 + \left\{ \frac{d\left\{ \frac{d}{dz} \left[\ln \frac{X(\lambda_1, Z)(\lambda_3, Z)}{X(\lambda_2, Z)^2} \right] \right\}}{d[X(\lambda_2, Z)]} \times u[X(\lambda_2, Z)] \right\}^2 + \left\{ \frac{d\left\{ \frac{d}{dz} \left[\ln \frac{X(\lambda_1, Z)(\lambda_3, Z)}{X(\lambda_2, Z)^2} \right] \right\}}{d[X(\lambda_3, Z)]} \times u[X(\lambda_3, Z)] \right\}^2}{N_N(Z) \Delta \sigma_N} \\
273 & \hspace{15em} (18)
\end{aligned}$$

274 where U_{NO_2} is NO_2 total retrieval relative uncertainty using three-wavelength DIAL technique;
275 U_{MED} , U_{OAD} , U_{AED} , U_B and U_s are NO_2 retrieval relative uncertainty caused by molecule,
276 absorption of gases other than the gas of interest, aerosol (extinction and backscattering) and
277 noise of lidar signals expressed as Eq. (14), (15), (16), (17) and (18); u is uncertainty function;
278 N_m and N_o are number density (ND) of air and ozone; σ_m is Rayleigh scattering cross section; σ_o
279 is absorption cross section of ozone; S is lidar ratio.

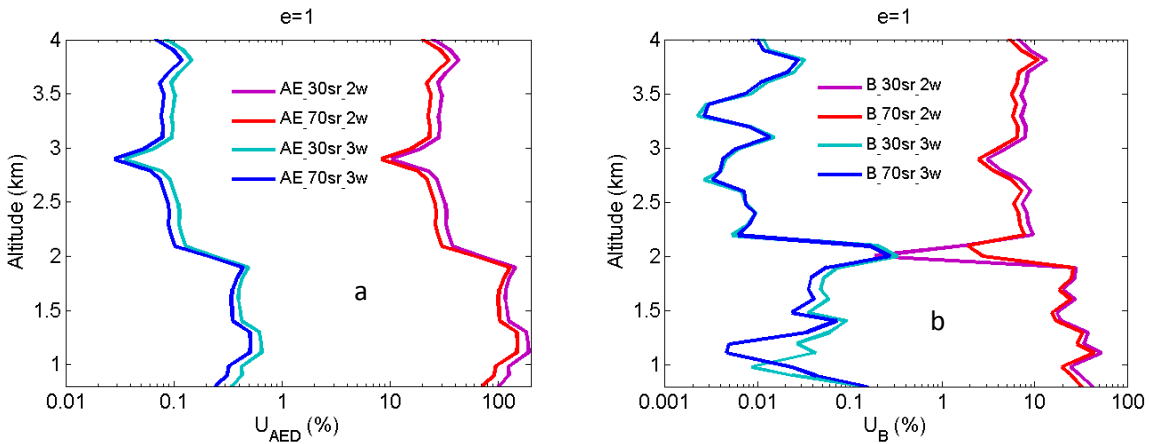
280 From Eq. (14) and (15), U_{MED} and U_{OAD} are determined by $u[N_m(z)]$ and $u[N_o(z)]$ (uncertainties
281 of N_m and N_o). In our measurements, profiles of temperature and pressure from local radiosonde
282 are used to calculate N_m . Usually, one radiosonde is launched for about 8-hour measurement.
283 One profile of air number density from local radiosonde is used to correct 8-hour NO_2
284 measurements. According to statistics of 8-hour variation of temperature and pressure in local
285 four seasons, the uncertainty of N_m is between 1% and 3%. U_{MED} using two-wavelength DIAL
286 technique and the three-wavelength DIAL technique are calculated according to Eq. (14) with
287 the uncertainty of N_a as 1%, 2% and 3% shown in Fig. 7(a). U_{MED} using three-wavelength DIAL
288 technique is far less than using two-wavelength DIAL technique. N_o is obtained from local
289 measurements. Because of very low values of ozone absorption cross section differentials, with
290 the uncertainty of N_o as 50% and 100%, U_{OAD} using two-wavelength DIAL technique and using
291 the three-wavelength DIAL technique are both less 0.5% from Fig.7 (b). Ozone absorption
292 correction is neglect in NO_2 retrieval. From Eq. (16) and (17), U_{AED} and U_B are determined by

293 uncertainties of a_a , β_a and e . For HU lidar system, 532-nm elastic signals are used to calculate a_a
294 and β_a with Fernald method to correct NO_2 retrieval [Fernald et al., 1972]. 50 sr is usually chosen
295 as lidar ratio to retrieve a_a and β_a . The lidar ratio is variable, so uncertainties of a_a and β_a are
296 caused by chosen lidar ratio. The range of lidar ratio is about from 30 sr to 70 sr for 532 nm. The
297 uncertainty of lidar ratio is 40% for 50 sr. The uncertainties of a_a and β_a are calculated with
298 uncertainty of lidar ratio as 40%. Finally, U_{AED} and U_B using two-wavelength DIAL technique
299 and using the three-wavelength DIAL technique are calculated with the Ångström exponent as 1,
300 2 and 3 shown in Fig. 8, 9 and 10. From these figures, U_{AED} and U_B using three-wavelength
301 DIAL technique are both less 4%. However, U_{AED} below 2 km using two-wavelength DIAL
302 technique are more than 90% after correction of aerosol extinction. From Eq. (18), U_s is
303 determined by uncertainties of three-wavelength lidar signals. The uncertainties of lidar signals
304 with average integration time of 1 minute and 2 minutes are derived from Poisson statistics
305 associated with the probability of detection of a repeated random event [Measures, 1984;
306 Leblanc et al., 2016]. NO_2 number density relative uncertainty owing to the noise of lidar signals
307 with average integration time of 1 minute and 2 minutes are obtained shown in Fig11. We can
308 see U_s using two-wavelength DIAL technique is smaller than using three-wavelength DIAL
309 technique. With increase of average integration time from 1 minute to 2 minutes, U_s can be
310 effectively reduced. At last, U_{NO_2} (the total relative uncertainties of NO_2) with e as 1, 2 and 3 are
311 calculated shown in Fig. 12(a), (b) and (c).



312

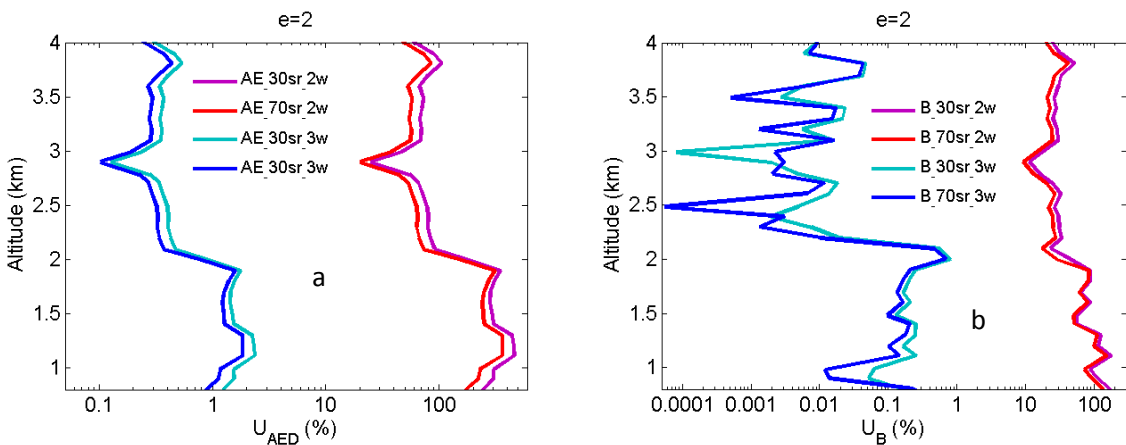
313 Fig.7 NO₂ number density relative uncertainty owing to air number density (a) and ozone number density
 314 (b).



315

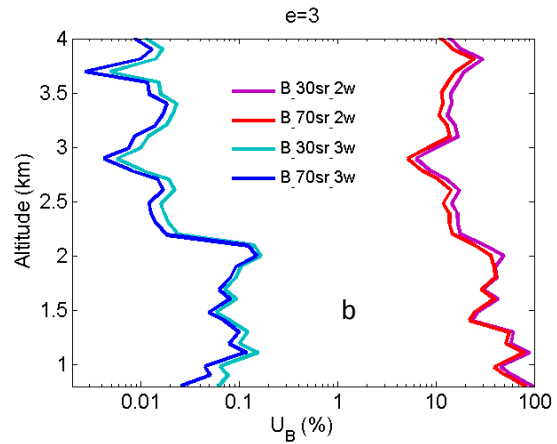
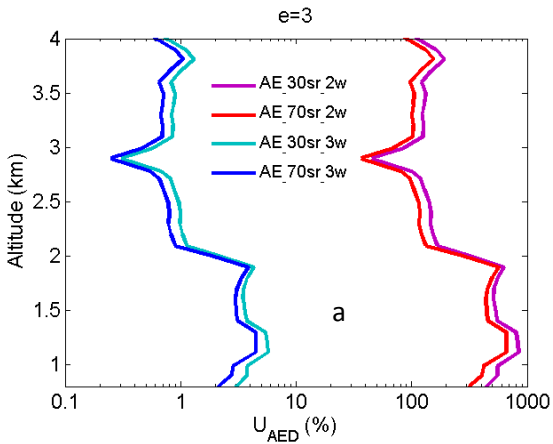
316 Fig.8 NO₂ number density relative uncertainty owing to aerosol extinction (a) and backscatter (b) with e=
 317 1.

318



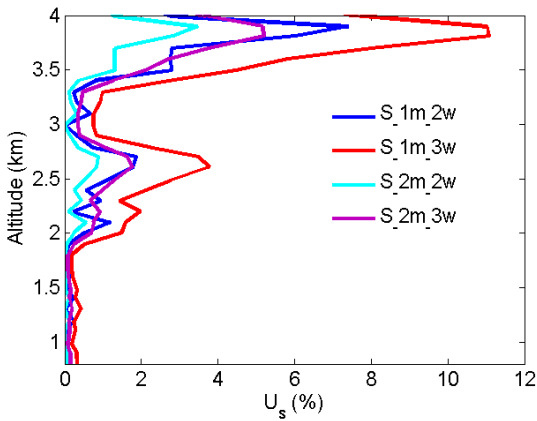
319

320 Fig.9 NO₂ number density relative uncertainty owing to aerosol extinction (a) and backscatter (b) with e=
 321 2.



322

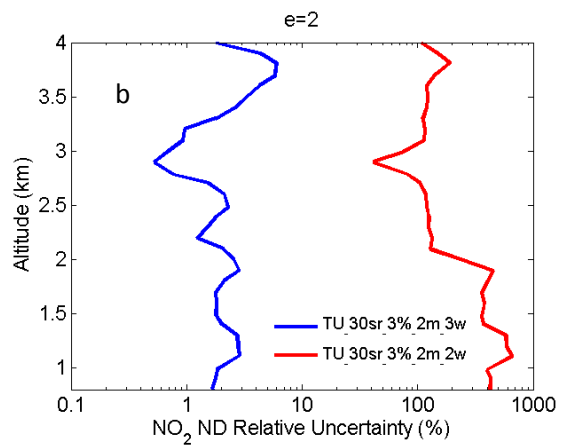
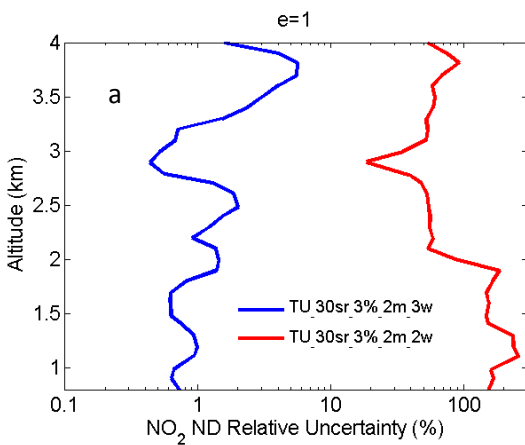
323 Fig.10 NO₂ number density relative uncertainty owing to aerosol extinction (a) and backscatter (b) with
324 e=3.



325

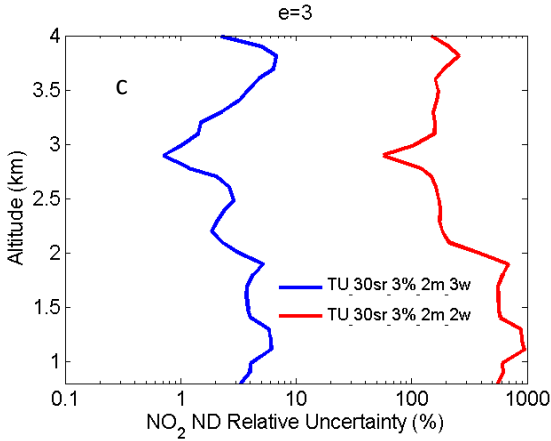
326 Fig.11 NO₂ number density relative uncertainty owing to the noise of signals with average of 1 minute
327 and 2 minutes.

328



329

330



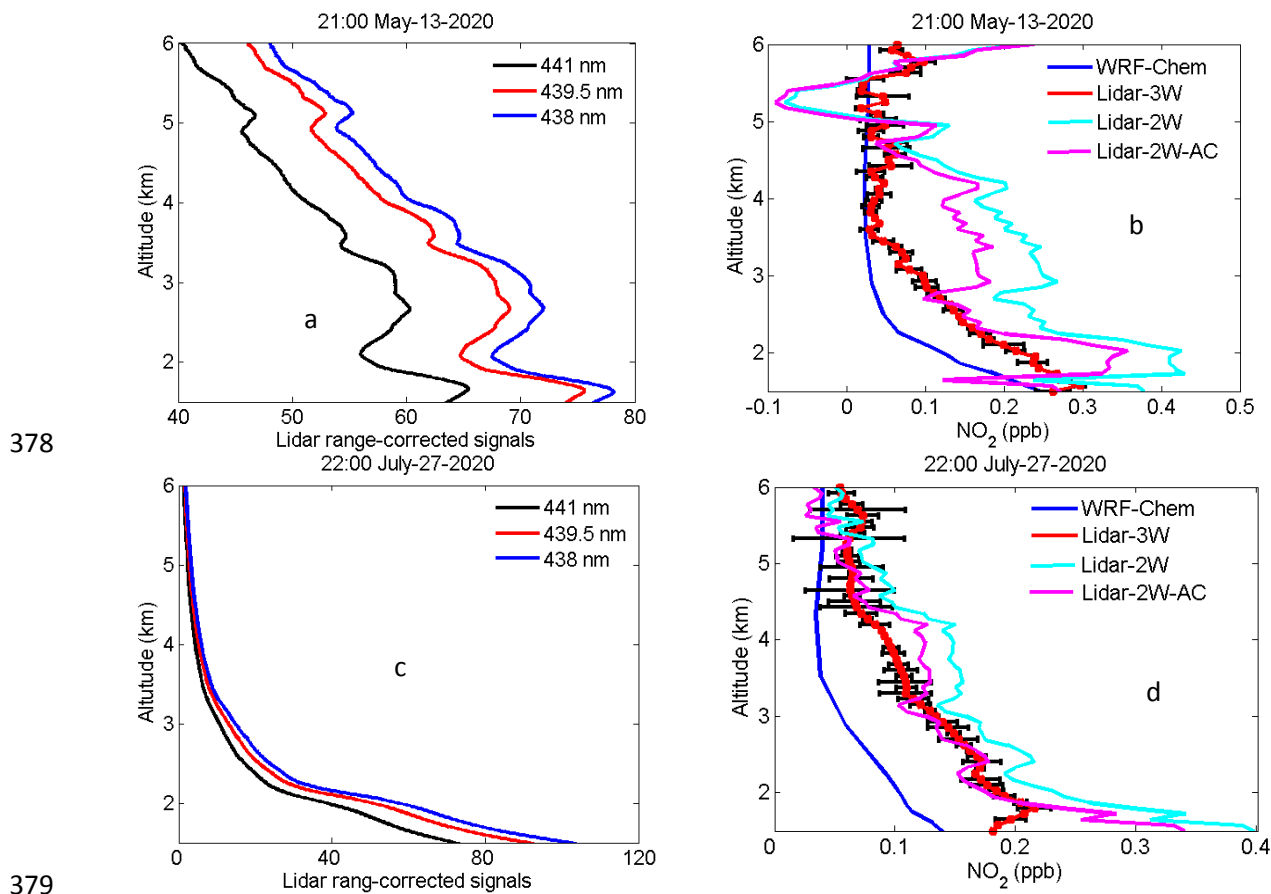
331
 332 Fig.12 NO₂ number density total relative uncertainty with e=1 (a), e=2 (b) and e=3 (c).

333
 334 **5. Results**

335 The three-wavelength DIAL technique was implemented by the HU lidar measurements during
 336 two cases at night and the resulting vertical profiles are presented in Fig. 13. All NO₂ lidar
 337 measurements presented here are obtained at times with less than 10% cloud coverage below 8
 338 km. HU lidar 438 nm (blue line), 439.5 nm (red line) and 441 nm (black line) elastic signals
 339 measured at 21:00 (local time) on May 13, 2020 and 22:00 (local time) on July 27, 2020 are
 340 shown in Fig. 13 (a) and (c), respectively. The average integration time for these signals is 2
 341 minutes. Determined from the lidar elastic signals in Fig. 13 (a) and (c), there is an existing
 342 aerosol layer between 2.2 km and 3.5 km on May 13, while July 27 presented a clean atmosphere.
 343 Fig. 13 (b) and (d) show retrieved NO₂ profiles using the three-wavelength DIAL technique (red
 344 line). The black error bars in Fig.13 (b) and (d) indicate the uncertainty of NO₂ retrieval
 345 calculated using Eq. (13). In Fig. 13 (b), the retrieved NO₂ profile between 2.2 km and 3.5 km on
 346 May 13 is smooth and not affected by the aerosol layer. The NO₂ profiles (sky-blue line and
 347 purple line) were also retrieved using the conventional two-wavelength DIAL technique without
 348 and with aerosol correction shown in Fig. 13 (b) resulting in a bump between 2.2 km and 3.5 km
 349 in the NO₂ profile retrieved using the two-wavelength DIAL technique. This inconsistency

350 suggests that the two-wavelength DIAL technique cannot remove AED of the aerosol layer
351 between 2.2 km and 3.5 km and the retrieved NO₂ profile contains AED interference. Moreover,
352 the NO₂ retrievals below 2 km using two-wavelength DIAL technique shown in Fig. 13 (b) and
353 (d) are more than the three-wavelength DIAL technique suggesting that the AED of boundary
354 aerosol was not correctly removed. Aerosol correction is very important for NO₂ retrieval using
355 the conventional two-wavelength DIAL technique [Browell et al., 1985]. These results suggest
356 that the proposed three-wavelength DIAL technique can effectively remove influence of aerosol
357 on the retrieval of NO₂. As a first-order assessment of the HU lidar NO₂ profiles, we compare the
358 retrieval results to simulated data from the Weather Research and Forecasting Chemistry (WRF-
359 Chem) model (Grell et al., 2005) at 12 km × 12 km spatial resolution and 200 m vertical
360 resolution. Past studies have demonstrated that WRF-Chem simulated NO₂ results show good
361 agreement between the OMI satellite measurements and aircraft measurements [Amnuaylojaroen
362 et al., 2019; Barten et al., 2020] providing a data source to examine the accuracy of the HU
363 retrievals using both two-wavelength DIAL technique and three-wavelength DIAL technique.
364 The HU local NO₂ profiles for these two cases are simulated using WRF-Chem model and
365 shown in Fig. 13 (b) and (d). WRF-Chem simulated NO₂ magnitudes tend to be lower compared
366 to HU retrieved NO₂ profiles using three-wavelength DIAL technique (typically within ±0.1
367 ppb), except above 3.5 km on May 13, 2020, however, the comparison demonstrates a consistent
368 vertical profile shape between observations and the model simulation. And retrieval results using
369 the three-wavelength DIAL technique are much closer to simulated values compared to using the
370 two-wavelength DIAL technique. These figures also demonstrate that the reduced fluctuations
371 caused by aerosol backscatter when using the three-wavelength DIAL technique results in
372 vertical profiles of NO₂ which are much more consistent with simulated data when compared to

373 results of the two-wavelength DIAL retrievals. Both the WRF-Chem simulated profiles and the
 374 HU retrievals of NO₂ using three-wavelength DIAL technique are associated with uncertainties
 375 which could result in the differences in magnitude; however, given the consistent nature in the
 376 vertical profile shapes from both data sources provides confidence that the HU lidar is retrieving
 377 NO₂ vertical profiles using three-wavelength DIAL technique in the troposphere.



380 Fig.13 HU lidar 438 nm, 439.5 nm and 441 nm elastic signals measured at 21:00 (local time) on May 13,
 381 2020 (a) and 22:00 (local time) on July 27, 2020 (c); NO₂ profiles obtained using three-wavelength DIAL
 382 technique, two-wavelength DIAL technique and WRF-Chem model at 21:00 on May 13, 2020 (b) and
 383 22:00 on July 27, 2020 (d).

384

385 6. Conclusion

386 This study describes a lidar retrieval technique using three wavelengths simultaneously emitted
 387 from an OPO laser to measure tropospheric NO₂ profiles. The three-wavelength DIAL retrieval

388 equations describe how the retrievals decrease errors caused by aerosol interference. Aerosol
389 extinction differences using this proposed technique can be decreased to less than 2% of aerosol
390 extinction differences resulting from a conventional two-wavelength DIAL technique.
391 Comparing the HU lidar results to WRF-Chem model output demonstrates that the NO₂
392 magnitudes and vertical structure are in much better agreement with simulated data when
393 applying the three-wavelength DIAL technique compared to using the two-wavelength technique.
394 In the future, we will add new filters to obtain daytime NO₂ measurements. We also plan to
395 purchase NO₂ balloonsondes for acquiring true validation data to evaluate HU lidar NO₂ results.

396

397 **Acknowledgments**

398 We thank NASA TOLNet and NASA DISCOVER-AQ measurements for our simulation work.
399 This study was supported by the PIRT project funded by US Army Research, Development and
400 Engineering Command (AQC) Center (DOD) under HU PIRT Award # 551150-211150) and the
401 National Oceanic and Atmospheric Administration- Cooperative Science Center for Earth
402 System and Sciences and Remote Sensing Technologies (NOAA-CESSRST) under the
403 Cooperative Agreement Grant #: NA16SEC4810008. The statements contained within the
404 manuscript/research article are not the opinions of the funding agency or the U.S. government,
405 but reflect the author's opinions. HU lidar data are available at [http://cas.hamptonu.edu/data-](http://cas.hamptonu.edu/data-products/)
406 [products/](http://cas.hamptonu.edu/data-products/). Matthew Johnson's contribution was supported by the NASA's TOLNet Science
407 Team and the Tropospheric Composition Program. We also thank Dr. Gabriele Pfister from the
408 Atmospheric Chemistry Observations & Modeling Lab at the National Center for Atmospheric
409 Research for providing the WRF-Chem calculation applied in this study.

410 **Supplementary Material**

411 S.1 Two-wavelength DIAL retrieval equation

Table s.1. Extinction and backscatter of molecule and aerosol for wavelengths of λ_1 and λ_2 .

wavelength	Molecular backscattering	Aerosol backscattering	Molecular extinction	Aerosol extinction
λ_1	$\left(\frac{\lambda_1}{\lambda_2}\right)^{-4} \beta_m$	$\left(\frac{\lambda_1}{\lambda_2}\right)^{-e} \beta_a$	$\left(\frac{\lambda_1}{\lambda_2}\right)^{-4} \alpha_m$	$\left(\frac{\lambda_1}{\lambda_2}\right)^{-e} \alpha_a$
λ_2	β_m	β_a	α_m	α_a

The two elastic lidar equations can be expressed as:

$$X(\lambda_1, Z) = C_1 \frac{\left[\left(\frac{\lambda_1}{\lambda_2}\right)^{-4} \beta_m(z) + \left(\frac{\lambda_2}{\lambda_1}\right)^{-e} \beta_a(z)\right]}{z^2} \exp\left\{-2 \int_0^Z \left[\left(\frac{\lambda_1}{\lambda_2}\right)^{-4} \alpha_m(z) + \left(\frac{\lambda_2}{\lambda_1}\right)^{-e} \alpha_a(z) + \sigma_N(\lambda_1, z) N_N(z) + O_{abs}(\lambda_1, z)\right] dz\right\} \quad (s.1)$$

$$X(\lambda_2, Z) = C_2 \frac{[\beta_m(z) + \beta_a(z)]}{z^2} \exp\{-2 \int_0^Z [\alpha_m(z) + \alpha_a(z) + \sigma_N(\lambda_2, z) N_N(z) + O_{abs}(\lambda_2, z)] dz\} \quad (s.2)$$

412 where X is the lidar signal; C_1 and C_2 are lidar constants; the subscripts a and m represent aerosol,
 413 and molecule, respectively; σ_N is the absorption cross section for the gas of interest; N_N is the
 414 molecular density of the gas of interest; O_{abs} is absorption of gases other than the gas of interest
 415 and z is the altitude. The molecular density of the gas of interest can be obtained after taking
 416 ratio of Eq. (1) to Eq. (2).

417 NO_2 density retrieval equation can be expressed as Eq. (3):

$$418 \quad N_N(Z) = \frac{\frac{1}{2} \times \frac{d}{dz} \left[\ln \frac{X(\lambda_1, Z)}{X(\lambda_2, Z)} \right] - AED(z) - MED(z) - OAD(z) - B(z)}{\Delta\sigma_N} \quad (s.3)$$

$$419 \quad \Delta\sigma_N = \sigma_N(\lambda_2) - \sigma_N(\lambda_1) \quad (s.4)$$

$$420 \quad B(z) = \frac{1}{2} \frac{d}{dz} \left[\ln \frac{\left(\frac{\lambda_1}{\lambda_2}\right)^{-4} \beta_m(z) + \left(\frac{\lambda_2}{\lambda_1}\right)^{-e} \beta_a(z)}{\beta_m(z) + \beta_a(z)} \right] \quad (s.5)$$

$$421 \quad AED(z) = \left[1 - \left(\frac{\lambda_1}{\lambda_2}\right)^{-e} \right] \alpha_a(z) \quad (s.6)$$

$$422 \quad MED(z) = \left[1 - \left(\frac{\lambda_1}{\lambda_2}\right)^{-4} \right] \alpha_m(z) \quad (s.7)$$

$$423 \quad OAD(z) = O_{abs}(\lambda_2, z) - O_{abs}(\lambda_1, z) \quad (s.8)$$

424 S.2 Units for all variables

425 Table s.2. Units for all variables

Items	Description	Unit
C1, C2,C3	lidar constant	constant (number)
α	extinction coefficient	km^{-1}
β	backscattering coefficient	$\text{km}^{-1}\text{sr}^{-1}$
λ	wavelength	nm
σ	absorption cross section	$\text{cm}^2\text{molecule}^{-1}$
Z, z	altitude	km
X	lidar range-corrected signal	mv
N	number density	$\text{molecule}/\text{cm}^3$
S	lidar ratio	sr^{-1}
U	Relative uncertainty	%

426

427 **Reference:**

428 Amnuaylojaroen T., Macatangay R.C., and Khodmanee S.: Modeling the effect of VOCs from
429 biomass burning emissions on ozone pollution in upper Southeast Asia, Heliyon., 5(10), e02661,
430 2019.

431 Barten, J. G. M., Ganzeveld, L. N., and Visser, A. J.: Rodrigo Jiménez, and Maarten C.Krol,
432 Evaluation of nitrogen oxides (NO_x) sources and sinks and ozone production in Colombia and
433 surrounding areas, Atmos. Chem. Phys., 20, 9441–9458, 2020.

434 Beirle, S., Boersma, K., Platt, U., Lawrence, M., and Wagner, T.: Megacity Emissions and
435 Lifetimes of Nitrogen Oxides Probed from Space, Science., 333, 1737–1739, 2011.

436 Beirle, S., Platt, U., Wenig, M., and Wagner, T.: Weekly cycle of NO_2 by GOME measurements:
437 a signature of anthropogenic sources, Atmos. Chem. Phys., 3(6), 2225–2232,2003.

438 Berg, N., Mellqvist, J., Jalkanen, J. P., and Balzani, J.: Ship emissions of SO_2 and NO_2 : DOAS
439 measurements from airborne platforms, Atmos. Meas. Tech., 5(5), 1085–1098, 2012.

440 Berglund, M., Boström, C. E., Bylin, G., Ewetz, L., Gustafsson, L., Moldéus, P., Norberg, S.,
441 Pershagen, G., and Victorin, K.: Health risk evaluation of nitrogen oxides, Scandinavian journal
442 of work: environment and health., 19, 1993.

443 Bertram, T. H., Heckel, A., Richter, A., Burrows, J. P., and Cohen, R. C.: Satellite measurements
444 of daily variations in soil NO_x emissions, Geophys. Res. Lett., 32, L24812, 2005.

445 Boersma, K. F., Jacob, D. J., Eskes, H. J., Pinder, R. W., Wang, J., and Van Der A, R. J.:
446 Intercomparison of SCIAMACHY and OMI tropospheric NO₂ columns: Observing the diurnal
447 evolution of chemistry and emissions from space, *J. Geophys. Res.*, 113, D16S26, 2008.

448 Bovensmann, H., Burrows, J. P., Buchwitz, M., Frerick, J., Noel, S., Rozanov, V. V., Chance, K.
449 V., and Goede, A. P. H.: SCIAMACHY: Mission objectives and measurement modes, *J. Atmos.*
450 *Sci.*, 56(2), 127–150, 1999.

451 Bucsela, E. J., et al.: Comparison of tropospheric NO₂ in situ aircraft measurements with near-
452 real-time and standard product data from the Ozone Monitoring Instrument, *J. Geophys. Res.*,
453 113, D16S31, doi:10.1029/2007JD008838, 2008.

454 Celarier, E. A., et al.: Validation of Ozone Monitoring Instrument nitrogen dioxide columns, *J.*
455 *Geophys. Res.*, 113, D15S15, doi:10.1029/ 2007JD008908, 2008.

456 Chen, Y., Jie Wang, Huang, J., and Hu, Shunxing. (2017). Measurement of atmospheric NO₂
457 profile using three-wavelength dual-differential absorption lidar, *Proc. SPIE.*, 10605, 106053L,
458 2017.

459 Cui, Y. Z., J. Lin, T., Song, C. Q., Liu, M. Y., Yan, Y. Y., Xu, Y., and Huang, B.: Rapid growth
460 in nitrogen dioxide pollution over Western China 2005-2013, *Atmos. Chem. Phys.*,16(10), 2016.

461 Edward V. B., Syed I., and Scott T. S.: Ultraviolet DIAL measurements of O₃ profiles in regions
462 of spatially inhomogeneous aerosols, *Appl. Opt.*, 24, 2827-2836,1985.

463 Fernald, F. G., Herman, B. M., and Reagan, J. A.: Determination of aerosol height distributions
464 by lidar, *Journal of Applied Meteorology.*, 11(3), 482-489, 1972

465 Fredriksson, K. A. and Hertz, H. M.: Evaluation of the DIAL technique for studies on NO₂
466 using a mobile lidarsystem, *Appl. Opt.*, 23(9), 1403–1411, 1984.

467 Georgoulas, A. K., Boersma, K. F., Vliet, J., Zhang, X., Ronald, A., Zani, P., and Laa, J.:
468 Detection of NO₂ pollution plumes from individual ships with the TROPOMI/S5P satellite
469 sensor, *Environ. Res. Lett.*, 15, 124037, 2020

470 Herman, J., Cede, A., Spinei, E., Mount, G., Tzortziou, M., and Abuhassan, N.: NO₂ column
471 amounts from ground-based Pandora and DOAS spectrometers using the direct-sun DOAS
472 technique: Intercomparisons and application to OMI validation, *J. Geophys. Res.*, 114(D13),
473 2009.

474 Kollonige, D. E., Thompson, A. M., Josipovic, M., Tzortziou, M., Beukes, J. P., Burger, R.,
475 Martins, D. K., van Zyl, P. G., Vakkari, V., and Laakso, L.: OMI satellite and ground - based
476 Pandora observations and their application to surface NO₂ estimations at terrestrial and marine
477 sites, *Journal of Geophysical Research.*, 123, 1441– 1459, 2018.

478 Kuang, S., M. J. Newchurch, J. Burris, and X. Liu (2013), Ground-based lidar for atmospheric
479 boundary layer ozone measurements, *Appl. Opt.*, 52, 3557-3566,
480 <http://dx.doi.org/10.1364/AO.52.003557>.

481 Kuang, S., Wang, B., Newchurch, M. J., Knupp, K., Tucker, P., Eloranta, E. W., Garcia, J. P.,
482 Razenkov, I., Sullivan, J. T., Berkoff, T. A., Gronoff, G., Lei, L., Senff, C. J., Langford, A. O.,
483 Leblanc, T., and Natraj, V.: Evaluation of UV aerosol retrievals from an ozone lidar, *Atmos.*
484 *Meas. Tech.*, 13, 5277–5292, <https://doi.org/10.5194/amt-13-5277-2020>, 2020.

485 Lamsal, L. N., et al.: Evaluation of OMI operational standard NO₂ column retrievals using in situ
486 and surface - based NO₂ observations, *Atmos. Chem. Phys.*, 14, 11,587 – 11,609, 2014.

487 Larkin, A., Geddes, J. A., Martin, R. V., Xiao, Q., Liu, Y., Marshall, J. D., Brauer, M., and
488 Hystad, P.: Global Land Use Regression Model for Nitrogen Dioxide Air Pollution.
489 *Environmental Science and Technology.*, 51(12), 6957-6964, 2017.

490 Leblanc, T., Sica, R. J., van Gijssel, J. A. E., Godin-Beekmann, S., Haeefele, A., Trickl, T., Payen,
491 G., and Liberti, G.: Proposed standardized definitions for vertical resolution and uncertainty in
492 the NDACC lidar ozone and temperature algorithms – Part 2: Ozone DIAL uncertainty budget,
493 *Atmos. Meas. Tech.*, 9, 4051–4078, <https://doi.org/10.5194/amt-9-4051-2016>, 2016.

494 Li, Z., Guo, J., Ding, A., Liao, H., Liu, J., Sun Y., Wang, T., Xue, H., Zhang, H., and Zhu, B.:
495 Aerosol and boundary-layer interactions and impact on air quality, *National Science Review.*,
496 4(6), 2017.

497 Liang, M., Guan, P., and Zheng, K.: Remote sensing of atmospheric NO₂ by employing the
498 continuous-wave differential absorption lidar technique, *Opt. Express.*, 25, A953-A962, 2017.

499 Liu, Q., Chen, Yafeng, J., Wang, J., Hu, S.: Measurement of atmospheric NO₂ profile using
500 three-wavelength dual-differential absorption lidar, *Proc. SPIE.*, 10605, LIDAR Imaging
501 Detection and Target Recognition, 106053L, 2017 <https://doi.org/10.1117/12.2295725>

502 Lorente, A. B., Boersma K. F., Eskes, H. J., Veefkind, J. P., Geffen, J. H. G. M., Zeeuw, M. B.,
503 Denier, H. A. C., Beirle, S., and Krol, M. C.: Quantification of nitrogen oxides emissions from

504 build-up of pollution over Paris with TROPOMI, *Sci Rep.*, 9, 20033, 2019,
505 <https://doi.org/10.1038/s41598-019-56428-5>,

506 Measures, R. M.: *Laser remote sensing: fundamentals and applications*, Wiley, 510, 1984.

507 Newchurch, M. J., Ayoub, M. A., Oltmans, S., Johnson, B., and Schmidlin, F. J.: Vertical
508 distribution of ozone at four sites in the United States, *J. Geophys. Res.*, 108(D1), 4031, 2003.

509 Reid, J. S., Kuehn, R. E., Holz, R. E., Eloranta, E. W., Kaku, K. C., Kuang, S., Newchurch, M. J.,
510 Thompson, A. M., Trepte, C. R., Zhang, J., Atwood, S. A., Hand, J. L., Holben, B. N., Minnis, P.,
511 and Posselt, D. J.: Ground based high spectral resolution lidar observation of aerosol vertical
512 distribution in the summertime Southeast United States, *J. Geophys. Res. Atmos.*, 122(2), 2970-
513 3004, 2017, doi:[10.1002/2016JD025798](https://doi.org/10.1002/2016JD025798).

514 Rothe, K. W., Brinkmann, U., and Walther, H.: Applications of tunable dye lasers to air pollution
515 detection: measurements of atmospheric NO₂ concentrations by differential absorption, *Appl.*
516 *Phys.*, 3(2), 1974.

517 Russell, A. R., Valin, L. C., and Cohen, R. C.: Trends in OMI NO₂ observations over the United
518 States: effects of emission control technology and the economic recession, *Atmos. Chem. Phys.*,
519 12, 12197–12209, <https://doi.org/10.5194/acp-12-12197-2012>, 2012.

520 Schuster, G., Dubovik, O., and Holben, B. N.: Ångström exponent and bimodal aerosol size
521 distributions, *J. Geophys. Res.*, 111, D07207, 2006.

522 Scott, D. C., Herman, R. L., Webster, C. R., May, R. D., Flesch, G. J., and Moyer, E. J.:
523 Airborne Laser Infrared Absorption Spectrometer (ALIAS-II) for in situ atmospheric
524 measurements of N₂O, CH₄, CO, HCL, and NO₂ from balloon or remotely piloted aircraft
525 platforms, *Appl. Opt.*, 38, 4609-4622, 1999.

526 Sluis, W. W., Allaart, M. A. F., Pitters, A. J. M., and Gast, L. F. L.: The development of a
527 nitrogen dioxide sonde, *Atmos. Meas. Tech.*, 3, 1753–1762, [https://doi.org/10.5194/amt-3-1753-](https://doi.org/10.5194/amt-3-1753-2010)
528 2010, 2010.

529 Sullivan, J., Rabenhorst, S. D., Dreessen, J., McGee, T. J., Delgado, R., Twigg, L., and Sumnicht,
530 G.: Lidar observations revealing transport of O₃ in the presence of a nocturnal low-level jet:
531 Regional implications for "next-day" pollution, *Atmospheric Environment.*, 158, 160-171, 2017.

532 Sullivan, J., McGee, T. J., Sumnicht, G. K., Twigg, L. W., and Hoff, R. M.: A mobile differential
533 absorption lidar to measure sub-hourly fluctuation of tropospheric ozone profiles in the
534 Baltimore–Washington, D.C. region, *Atmos. Meas. Tech.*, 7, 3529–3548, 2014.

535 Sunesson, J. A.: Differential absorption lidar system for routine monitoring of tropospheric
536 ozone, *Appl. Opt.*, 33(30), 7045-7058, 1994.

537 U.S. EPA 2016. Climate change indicators in the United States, 2016. Fourth edition. EPA 430-
538 R-16-004.

539 U.S. EPA 2018. Data from the Air Pollutant Emission Trends Data website. Accessed 2018.
540 <https://www.epa.gov/air-emissions-inventories/air-pollutant-emissions-trends-data>.

541 Valks, P., Pinardi, G., Richter, A., Lambert, J. C., Hao, N., Loyola, D., Van Roozendael, M., and
542 Emmadi, S.: Operational total and tropospheric NO₂ column retrieval for GOME-2, *Atmos.*
543 *Meas. Tech.*, 4(7), 1491–1514, 2011.

544 Volten, H., Brinksma, E. J., Berkhout, A. J. C., Hains, J., Bergwerff, J. B., Van der Hoff, G.
545 R., Apituley, A., Dirksen, R. J., Calabretta, J. S., and Swart, D. P. J.: NO₂ lidar profile
546 measurements for satellite interpretation and validation, *Journal of Geophysical Research.*,
547 114(24), 2009.

548 Wang, Z., Nakane, H., Hu, H., and Zhou J.: Three-wavelength dual differential absorption lidar
549 method for stratospheric ozone measurements in the presence of volcanic aerosols, *Appl. Opt.*,
550 36, 1245-1252, 1997.

551 Weibring, P., Smith, J. N., Edner, H., and Svanberg, S.: Development and testing of a frequency-
552 agile optical parametric oscillator system for differential absorption lidar, *Review of Scientific*
553 *Instruments.*, 74, 4478, 2003.